metals

MDPI

Article

Evolutions on Microstructure and Impact Toughness of G115 Steel after Long-Term Aging at 700 °C

Jianming Yu †, Shaohai Ma †, Kui Liang, Kai Yan *, Xisheng Yang and Shuli Zhang

China Special Equipment Inspection and Research Institute, Beijing 100029, China; yujianming@csei.org.cn (J.Y.); mashaohai@csei.org.cn (S.M.); liangkui@csei.org.cn (K.L.); yangxisheng@csei.org.cn (X.Y.); zhangshuli@csei.org.cn (S.Z.)

* Correspondence: yankai@csei.org.cn

† These authors contributed equally to this work.

Abstract: The microstructure and impact toughness evolution of G115 steel after long-term (ranging from 500 h to 10,000 h) aging at 700 °C were investigated in this study. The results showed that the microstructure of the G115 steel evolved from a finer-grained matrix with minor precipitates to a coarse-grained matrix with more precipitate with aging time, presenting a decrease in the local deformation degree in the matrix. The impact toughness of the steel decreased with aging time, presenting the largest decline at the initial aging times. The decrease in impact toughness was attributed to the coarsening of precipitates ($M_{23}C_6$ and Laves phase) in the steel matrix. The stable impact toughness during the whole aging process (from 500 h to 10,000 h) should be related to the comprehensive effects, including the precipitation of the Laves phase, the increase in high-angle grain boundaries, and the softening of the metal matrix.

Keywords: aging process at high temperature; martensitic steels; precipitates; toughness

check for updates

Citation: Yu, J.; Ma, S.; Liang, K.; Yan, K.; Yang, X.; Zhang, S. Evolutions on Microstructure and Impact Toughness of G115 Steel after Long-Term Aging at 700 °C. *Metals* **2024**, *14*, 921. https://doi.org/10.3390/met14080921

Academic Editor: Koh-ichi Sugimoto

Received: 9 July 2024
Revised: 1 August 2024
Accepted: 12 August 2024
Published: 14 August 2024

Copyright: © 2024 by the authors. Licensee MDPI, Basel, Switzerland. This article is an open access article distributed under the terms and conditions of the Creative Commons Attribution (CC BY) license (https://creativecommons.org/licenses/by/4.0/).

1. Introduction

Reducing CO_2 emissions and improving the efficiency of coal-fired power plants are crucial for promoting the development of the power industry [1–4]. Ultra-supercritical (USC) power plants as the focus of research and development around the world are an efficient method, involving coal-fired power with an operating temperature ranging from 650 °C to 750 °C [5–9]. However, coal-fired power plants mostly operate at temperatures below 600 °C, which poses a challenge for the traditional 9–12%Cr ferritic steels used in thick-section boiler components for USC [10–14]. Additionally, 9–12%Cr ferritic steels present excellent resistance to high-temperature oxidation, which is mainly attributed to the formation of Cr_2O_3 in the oxide layer [1,3,6,8,14]. It is necessary to simultaneously consider the antioxidant performance and high-temperature mechanical properties during the operation of the USC [4,9–11]. ASME-grade T/P92 (9Cr-1.8W-0.5Mo-NbV) is a specific version of 9%Cr heat-resistant steel [13,14]. V and Nb were added to enhance its creep strength, and the Cr content was raised to have better oxidation resistance [15]. Due to the elevated power generation parameters (high temperature and high pressure), there is often a problem of toughness reduction caused by coarse grain size. On the basis of traditional 9Cr steel, by increasing the W content, no more Mo was added, and B, Co, and Cu were added, and excellent creep resistance at high temperature was ultimately achieved [11,15–21]. G115 martensitic steel (9Cr-3W-3Co steels) is known for its excellent mechanical properties, including high strength, high toughness, and good resistance to corrosion and fatigue. The addition of W and Mo as well as optimization of other alloying elements offer T/P92 steel higher creep rupture strength compared with the older T/P91 steel. Steam generators and their components are often subjected to repeated thermal stress as a result of the temperature gradients that occur during start-ups and shutdowns

or during temperature transients. Thus, the risk of fatigue failure for the G115 steel increases under plastic deformation conditions, especially at high temperatures, which can have a significant impact on the structural integrity and reliability of components made from this material [11,15]. The effects of alloying elements and applied temperature on the strength of G115 steel have been reported, and it was found that the formed Laves phases [11,14], M_xC_Y (M-Cr and Fe elements) [11,14,19–21] and MX (M-Ni and Ti elements) [22–24] precipitates present combinations of various amounts and sizes, which can be sites of local fracture or key obstacles to the dislocation movement. However, the toughness evolution and the mechanism of G115 steel under long-term aging conditions at ultra-high temperatures (650–750 °C) is not clarified, which is one of the critical factors affecting the high-temperature operation process. It is necessary to explore the relationship between microstructural evolution and mechanical properties in G115 steel under various aging conditions.

This study investigated the evolution of microstructure and toughness in aged G115 steel. Figuring out the effects of the aging process on the toughness of the steel is crucial for material selection and component design, especially in applications for USC, where a balance between the service temperature and toughness is required.

2. Materials and Experiments

The experimental G115 steel was obtained after the casting and the hot forging processes, and its chemical composition is made up of C 0.08, Si 0.34, Mn 0.55, Cr 8.98, W 2.72, Co 3.01, V 0.21, Nb 0.05, Cu 0.96, and Fe balance (Central Iron & Steel Research Institute, Beijing, China). Before tests, the G115 steel as the base material (BM) was normalized at 1100 °C for 2 h with air cooling, and then tempered at 780 °C for 2 h with air cooling. After the gradual grinding and polishing processes with abrasive papers and 0.5 μm diamond paste, the microstructures of specimens after aging at 700 °C for 500 h, 1000 h, 3000 h, 5000 h, and 10,000 h were characterized by an optical microscope (OM) and a field emission scanning electron microscope (FESEM). The grain size of specimens after the aging processes was measured by Image-Pro Plus 6.0 software in SEM images. After the electrolytic double-spray process in the solution mixed with 10 vol.% perchloric acid and 90% alcohol, the electron back-scattered diffraction (EBSD) technique was used for characterizing the proportion of the low-angle grain boundaries (LAGBs), high-angle grain boundaries (HAGBs), the phase composition, the proportion of recrystallization microstructure, and the local plastic deformation in specimens after long-term aging processes with different times. The M23C6, MX, LP particles, and the lath martensite were characterized in the thin foils of G115 steel by using the TECNALG220 (Eindhoven, The Netherlands) field emission transmission electron microscope (FETEM) at 200 kV, and the testing specimens were prepared through the same method with the EBSD test.

As shown in Figure 1, Charpy impact tests were performed on the V-shaped notch specimen in accordance with the GB/T 229-2007 standard [25] by using a Charpy impact tester (ZBC2452-CD, SANS, Shenzhen, China) with a 200 kg load, and all tests were maintained at room temperature (20–22 °C). The impact toughness (K_V) was calculated using the following formula [25,26]:

$$Kv = (P \times L)/(2W) \quad (1)$$

where P is the load at failure, L is the length of the specimen, and W is the width of the specimen. For each test after the aging process, three specimens were carried out and the average value of the data was obtained. The neck portions of ruptured specimens were observed by FESEM to illustrate the fracture mode.

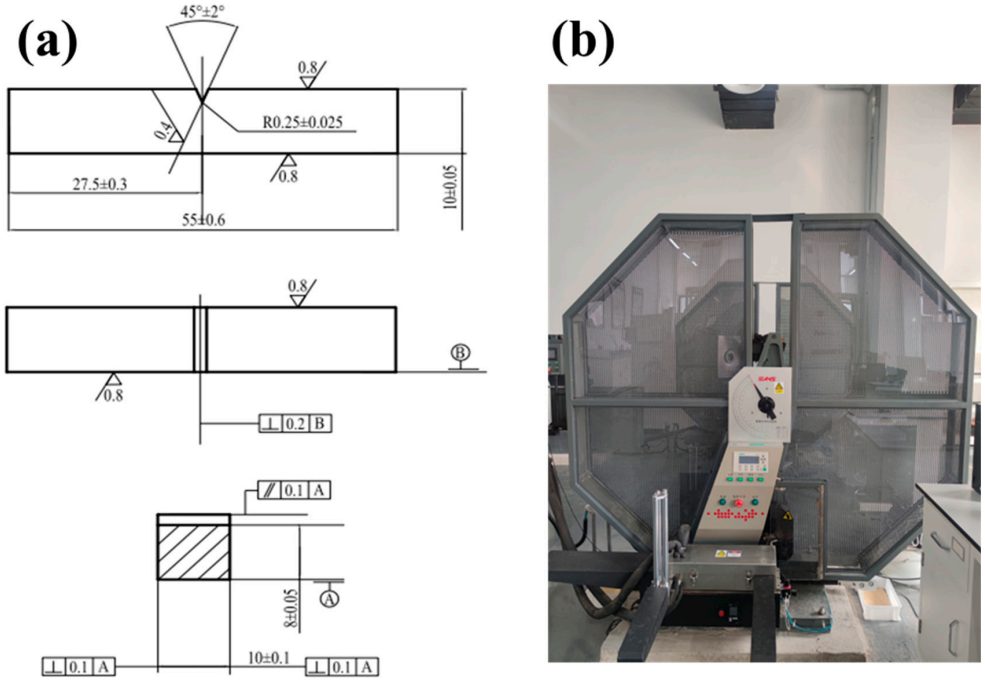


Figure 1. (**a**) Schematic diagram of the impact specimen (unit: mm). (**b**) The ZBC2452-CD Charpy impact tester.

3. Results

3.1. Microstructure

Figure 2 displays the metallographic microstructure of steels after etching in a mixed solution consisting of $FeCl_3$ (5 g), HCl (15 mL), and H_2O (80 mL) for 45 s. Obviously, the steel matrix was composed of lath martensite, including the prior austenite grains (PAGs). With increasing aging time, the grain grew and coarsened with the increasing width of lath martensite [16,19,27]. It can be observed that both the grain size and the width of lath martensite increased for specimens after the aging processes from 500 h to 10,000 h. The increasing size of PAG gradually led to unclear grain boundaries and the prolongation of lath martensite.

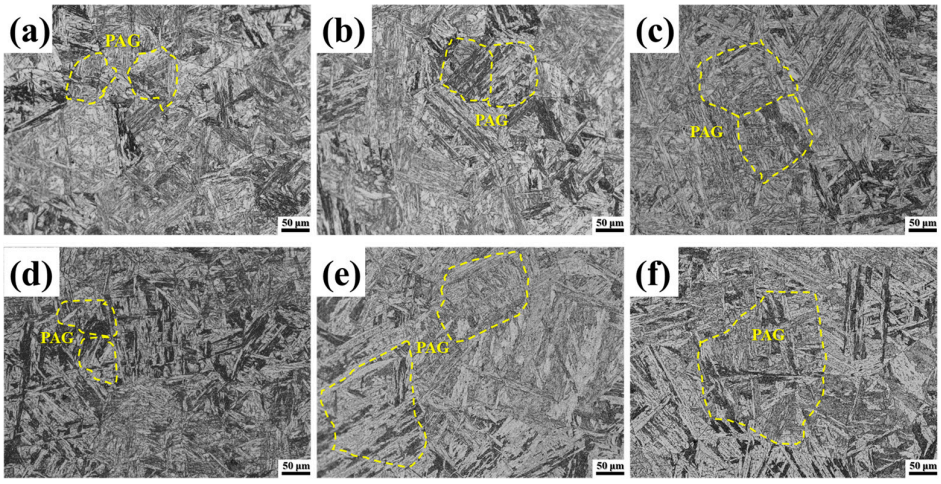


Figure 2. Metallographic morphology of G115 steel with different aging times at 700 °C: (**a**) BM, (**b**) 500 h, (**c**) 1000 h, (**d**) 3000 h, (**e**) 5000 h, (**f**) 10,000 h; PAGs are marked in images.

The grain size evolution of PAG in G115 steel after different aging times is shown in Figure 3, which was measured at three zones containing about 60 grains. It can be found

that the grain size of G115 steel is basically the same among the BM, the steel after aging 500 h, the steel after aging 1000 h, and the steel after aging 3000 h, and the average grain size of specimens ranges from 25.5 μm to 26.6 μm. After 5000 h aging time, the average grain size of G115 steel increased obviously to about 30 μm, corresponding to the broadening behavior of lath martensite [19,28,29]. Further, the average grain size of the G115 steel after 10,000 h aging time is about 32 μm, which indicates that the aging process promoted the growth of PAG in G115 steel.

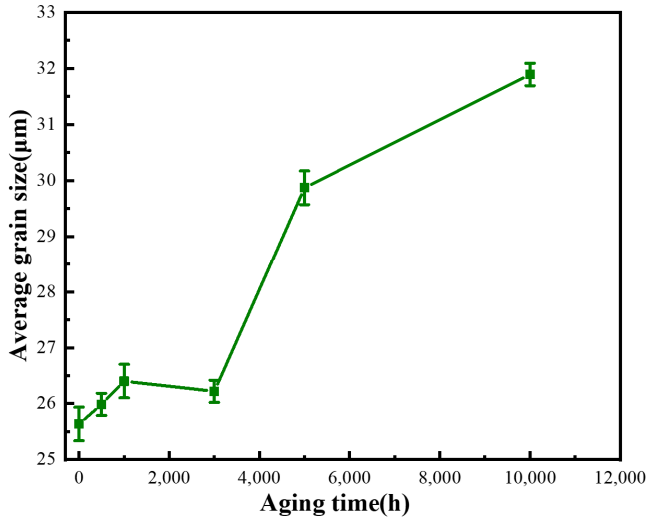


Figure 3. Average grain size of PAG in G115 steel with different aging times at 700 °C.

Figure 4 presents the SEM images of G115 steel after different aging times. It can be found that the length of lath martensite was limited by the grain size of PAG. The lath martensite gradually grew with the increase in aging time, which should be related to the reduction in dislocation density during the long-term aging process [7,18]. As for the specimens before 3000 h, the martensitic plates can be observed in PAG, presenting different degrees of broadening. Meanwhile, the same polygonal sub-grain structures can be found in PAG for the specimens after 5000 h and 10,000 h aging time. It has been recognized that the stability of the lath structure mainly depends on the pinning effect of dislocation and fine precipitates, which need further discussion compared with EBSD and TEM results.

Figure 5 shows the magnified back-scattered electron (BSE) images of each specimen, which was used for characterizing the precipitate and second particles in G115 steel after the long-term aging process. According to the mean size of MX (20–50 nm), $M_{23}C_6$ (100–400 nm), and Laves phase (100–400 nm) particles and the distribution sites [11,15,21], the particles can be roughly identified in steel. It can be found that $M_{23}C_6$ carbides were the main composition in all steels, which were mainly distributed at the grain boundaries and the martensitic lath boundaries. The presence of $M_{23}C_6$ carbides showed that these carbides became coarser and more distributed throughout the microstructure as aging time increased [12–17]. The microstructure of G115 steel is initially characterized by a fine-grained matrix. However, as the steel is aged at 700 °C, the precipitates within the matrix begin to grow and coarsen. The coarsening of precipitates was attributed to the diffusion of alloying element atoms and the thermodynamic drive, which achieved a more homogeneous microstructure. The growth of precipitates led to more extensive precipitate coverage in the matrix, which can potentially enhance the strength of the material but may compromise its toughness. It has been reported that $M_{23}C_6$ is $Cr_{23}C_6$ and the Laves phase is mainly Fe_2W [15,18]. Due to the heavier atom weight of W than Cr, the Laves phase is brighter than $M_{23}C_6$ in BSE images, which can be used to distinguish the Laves phase from $M_{23}C_6$ particles [11]. The growth of $M_{23}C_6$ and the Laves phase at grain boundaries during the aging process should influence the impact toughness, which needs further discussion.

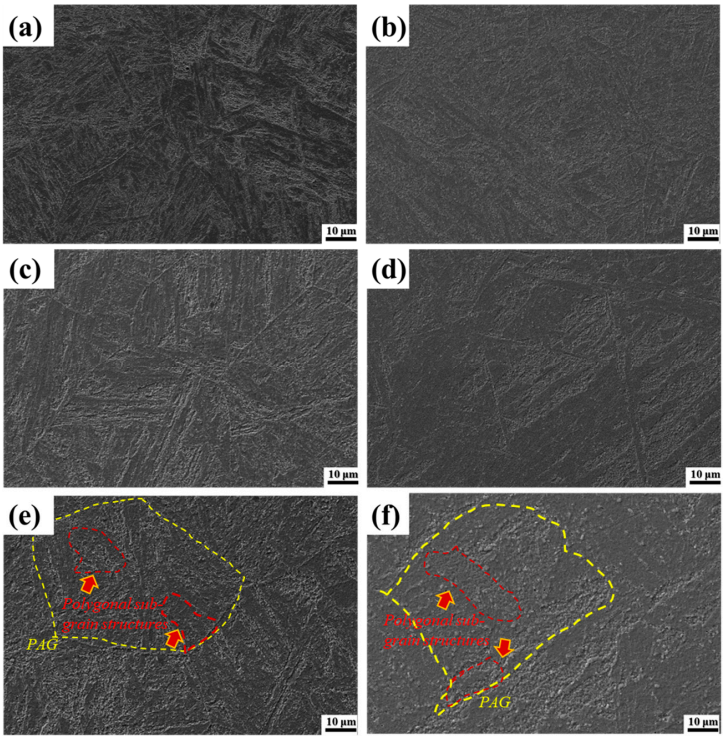


Figure 4. SEM morphologies of G115 steel with different aging times at 700 °C: (**a**) BM, (**b**) 500 h, (**c**) 1000 h, (**d**) 3000 h, (**e**) 5000 h, (**f**) 10,000 h.

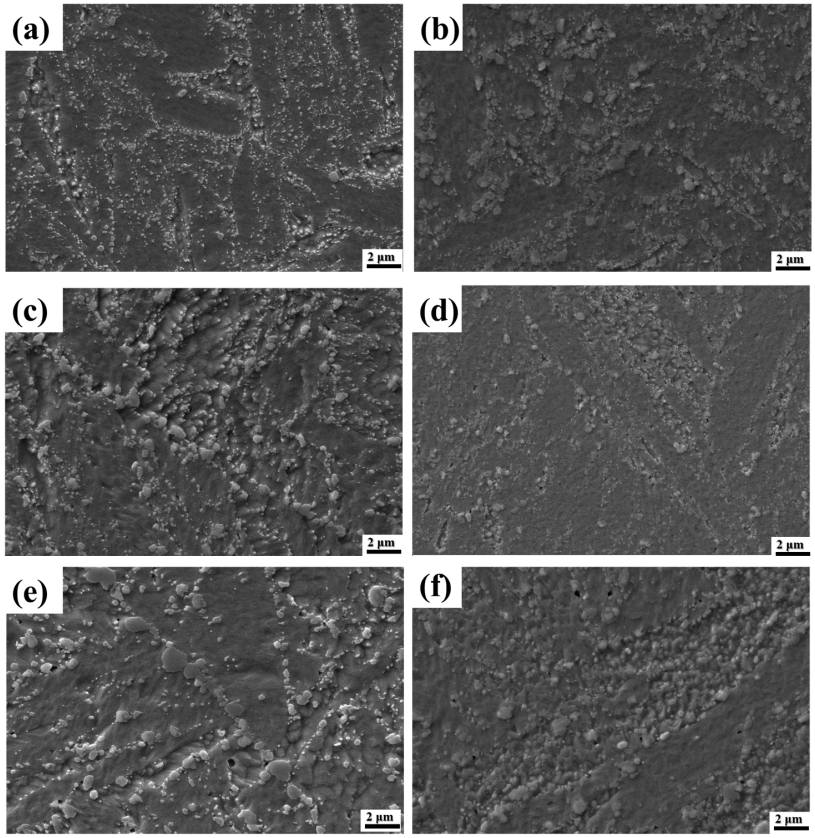


Figure 5. Magnified back-scattered electron morphologies of G115 steel with different aging times at 700 °C: (**a**) BM, (**b**) 500 h, (**c**) 1000 h, (**d**) 3000 h, (**e**) 5000 h, (**f**) 10,000 h.

3.2. EBSD Characterizations

To investigate the orientation of microstructures and the recrystallization degree for the BM and the G115 steel after 3000 h, 5000 h, and 10,000 h aging times, the EBSD maps are shown in Figure 6. The random orientation of microstructures was found in the inverse pole figures (IPFs) for all steels. Grain orientation spread (GOS) maps were used to characterize the fraction of recrystallized structure in G115 steel during the aging processes. As for BM, the fraction of grain with GOS less than 1° is 0.064, indicating the lower recrystallization degree for the original G115. With the duration of aging time, the faction of grain with low GOS (<1°) presents a slight increase (from 0.064 to 0.092), which should be related to the local stress release [13,16,19].

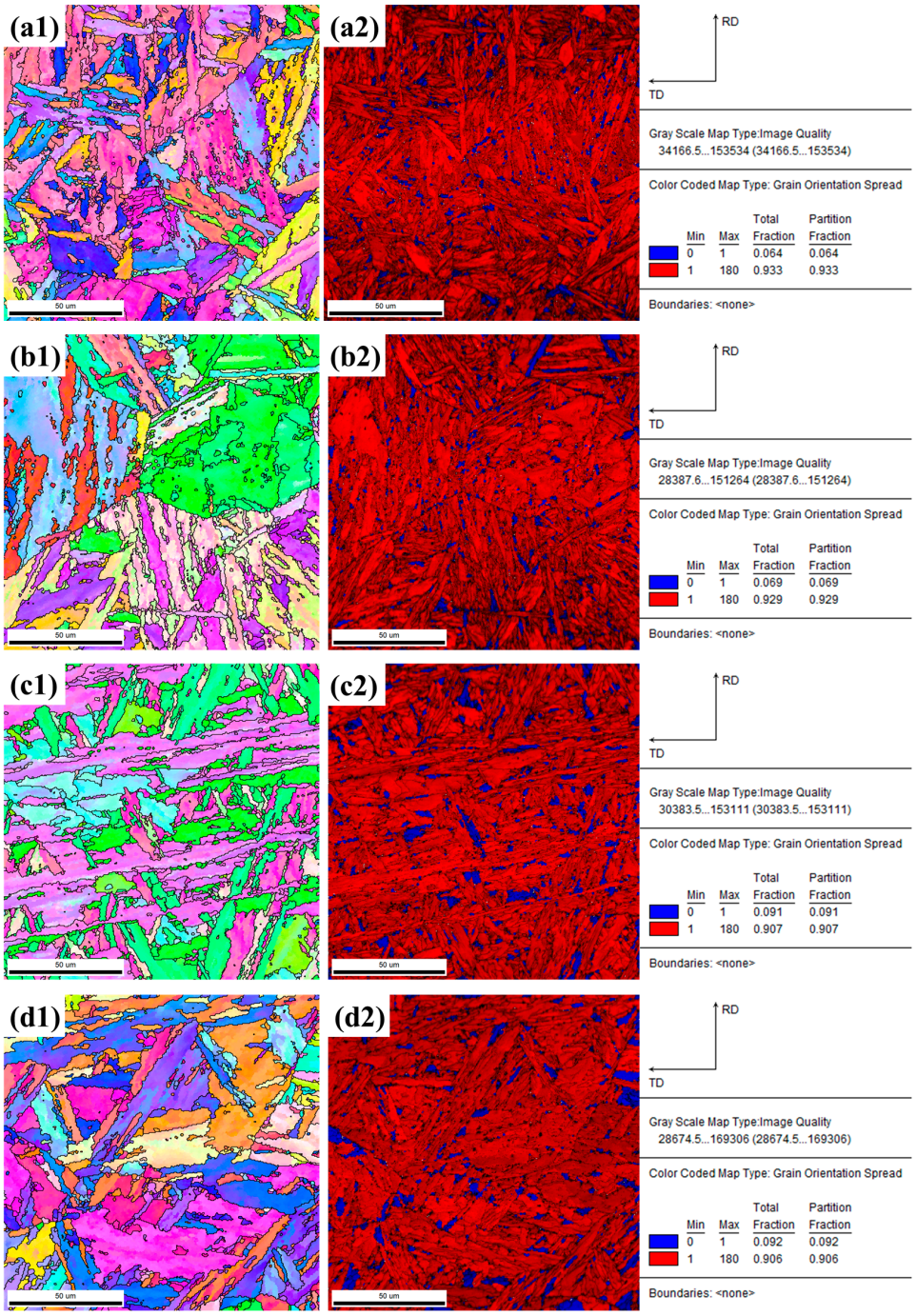


Figure 6. EBSD maps of G115 steel with different aging times at 700 °C: (**a**) BM, (**b**) 3000 h, (**c**) 5000 h, (**d**) 10,000 h, (**1**) inverse pole figures and (**2**) grain orientation spread maps.

Further, the grain boundary misorientation angle distribution of the BM and the G115 steel after 3000 h, 5000 h, and 10,000 h aging times is characterized by the EBSD technique, as shown in Figure 7. In the maps, black lines denote high-angle grain boundaries (HAGBs) for misorientation angles > 15°, and red lines represent low-angle grain boundaries (LAGBs) for values between 2° and 15° [12,18]. It can be found that the proportion of HAGB gradually increases from about 0.35 of BM and the steel after 3000 h aging time to 0.40 of the steel after 5000 h aging time [11]. The proportion of HAGB for the steel after 10,000 h aging time is about 0.39, which is slightly lower than that of the steel after 3000 h. It should be related to the formation of some precipitates and second-phase particles.

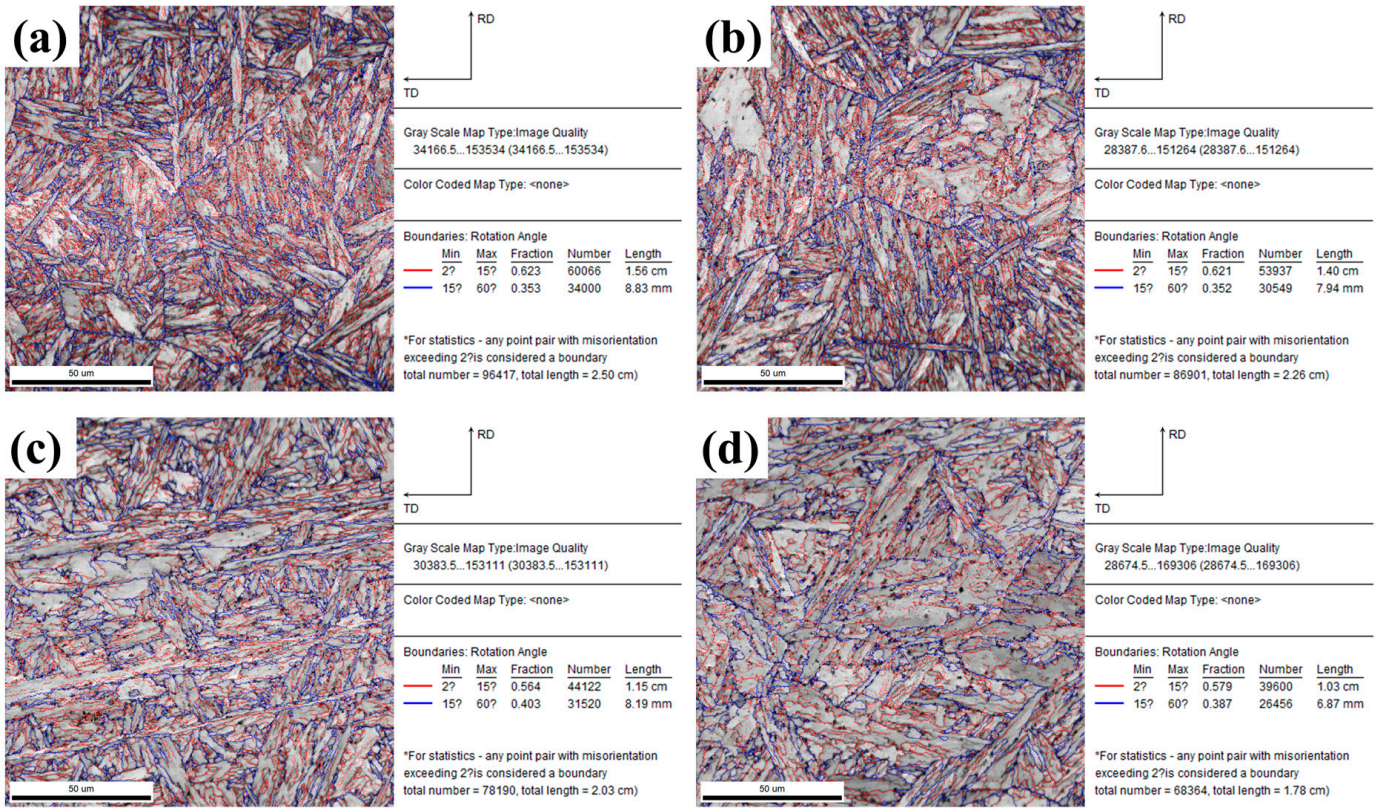


Figure 7. Grain boundary distribution maps of the G115 steel with different aging times at 700 °C: (**a**) BM, (**b**) 3000 h, (**c**) 5000 h, (**d**) 10,000 h.

To obtain the evolution of local misorientation distributions of G115 steel during the aging process, kernel average misorientation (KAM) maps were used (Figure 8). The yellow area (KAM = 1–3) is given special attention in the map, which can reflect the local deformation. With the aging time, the fraction of yellow area in G115 steel gradually decreased (from 0.47 of BM to 0.24 of steel after 10,000 h aging time), and the local orientation distributions were homogeneous, which implied that the recrystallization of the microstructure occurred during the aging process [11,16], leading to the local stress release.

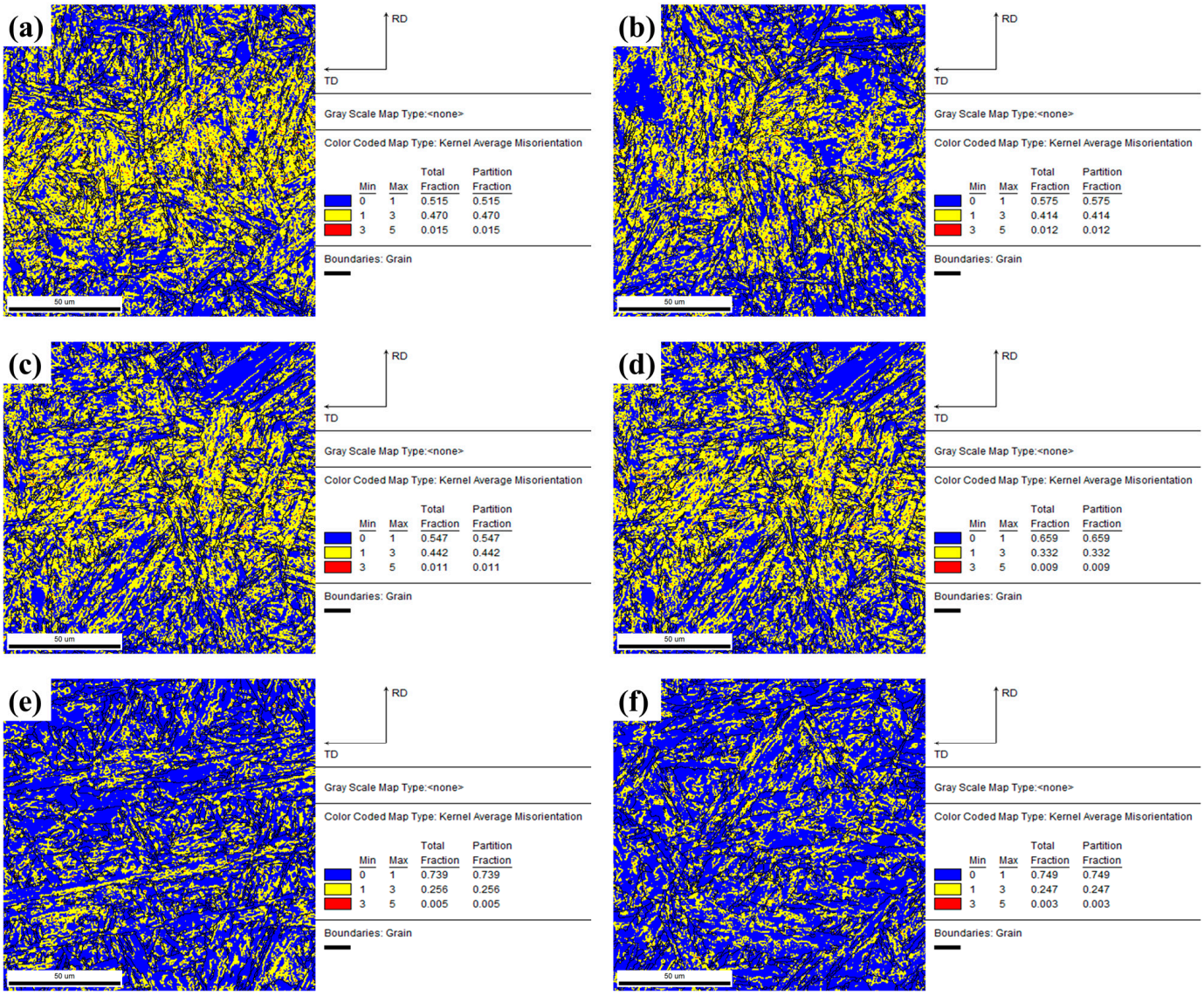


Figure 8. Kernel average misorientation maps of the G115 steel with different aging times at 700 °C: (**a**) BM, (**b**) 500 h, (**c**) 1000 h, (**d**) 3000 d, (**e**) 5000 h, (**f**) 10,000 h.

3.3. TEM Observation

Figure 9 shows the TEM images of G115 steel with different aging times at 700 °C. The slender and fragmentized laths can be found in BM with some particles distributed at the boundaries of martensitic lath. It can be confirmed that these particles are mainly composed of $Cr_{23}C_6$ and Fe_2W (Laves phase), and the MX precipitates can hardly be found in the matrix [15]. After 3000 h aging time, the width of the martensite lath structures increased, and the size of particles increased obviously compared with BM. The content of W and Fe increased, which indicates the growth of Laves phases during the aging process. As for the G115 after aging for 5000 h at 700 °C, the size of Laves phase particles significantly increased based on the SEM and EDS results. For the G115 after aging for 10,000 h at 700 °C, the particles of G115 steel are $Cr_{23}C_6$ precipitates, which can be confirmed by EDS results. The martensite lath structures became fuzzy in the G115 steel after the long-term aging process (5000 h and 100,000 h). The evolution of these microstructures should influence the impact toughness of G115, which needs further discussion.

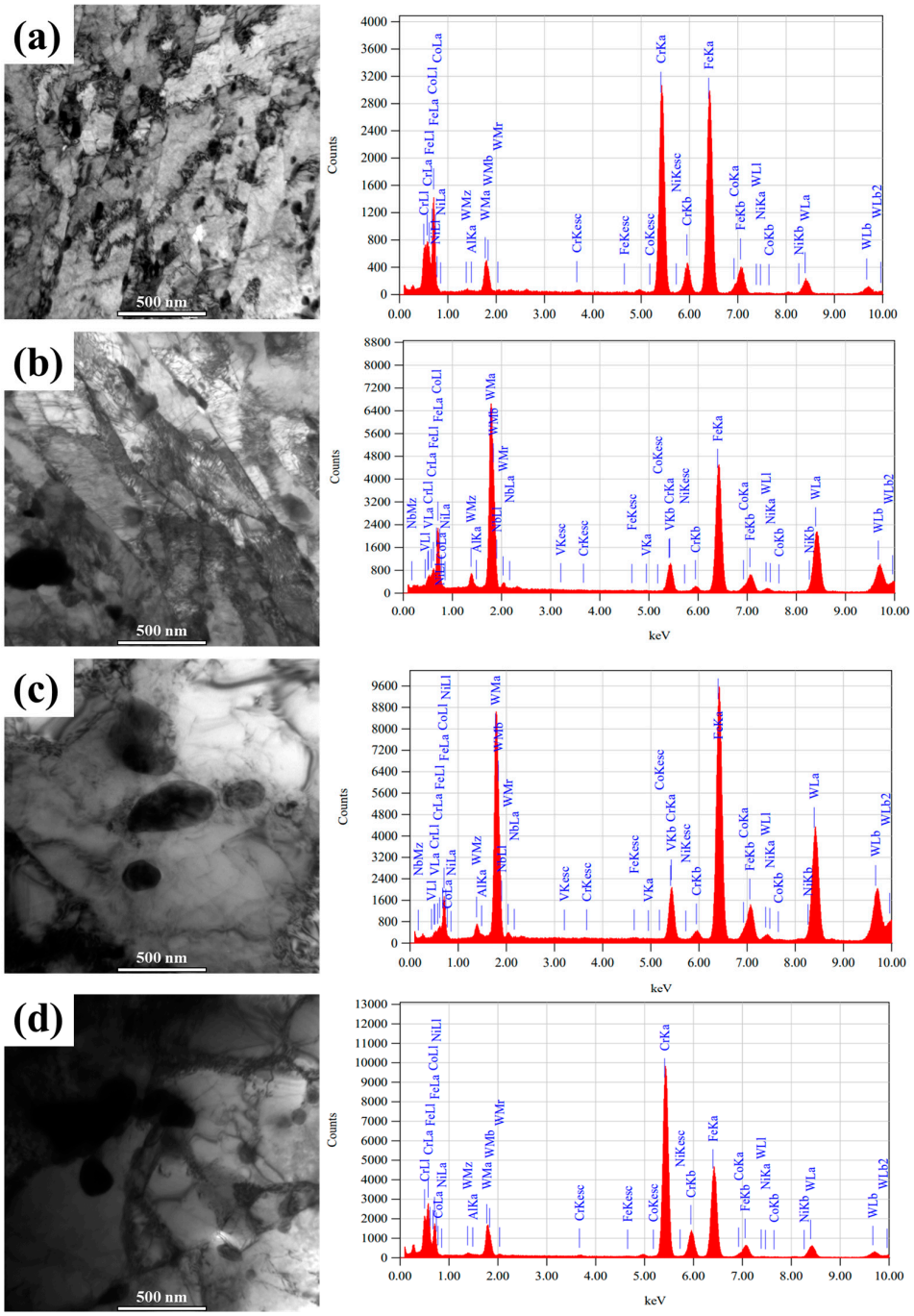


Figure 9. TEM images of G115 steel with different aging times at 700 °C: (**a**) BM, (**b**) 3000 h, (**c**) 5000 h, (**d**) 10,000 h; EDS results were obtained at the local area.

3.4. Impact Toughness Evolution and Analysis

Figure 10 shows the toughness values of the G115 steel after long-term aging at 700 °C, and the statistical analysis of the impact toughness results can be seen in Table 1. The mean values of impact energy were 51.3 J for BM, 17.4 J for 500 h, 18.2 J for 1000 h, 19.6 J for 3000 h, 16.7 J for 5000 h, and 15.7 J for 10,000 h. The impact energy decreased quickly after 500 h, and maintained a basically unchanged state until 10,000 h. The decreased impact toughness of the G115 steel with aging time indicates a potential reduction in the resistance to plastic deformation and crack elongation. The decline in impact toughness was significant after the aging process at 700 °C, suggesting that the microstructural changes had a pronounced effect on the toughness. The decrease in impact toughness

was attributed to the coarsening of precipitates, which provided fewer barriers to crack propagation. The development of microvoids within the steel matrix acted as potential sites for crack initiation [17]. The decline in impact toughness at the initial aging time is significant. Generally, the impact toughness can be an evaluation of its ability to resist crack propagation under high-stress and high-temperature conditions. In the case of G115 steel, the coarsening of precipitates and the development of microvoids are believed to be the primary causes of the decrease in impact toughness [11]. The larger precipitates can act as initiation sites for crack formation, and the microvoids can serve as paths for crack propagation, which reduces the overall resistance to impact for steel. The sharp drops in toughness after the 500 h aging process at 700 °C should be attributed to the appearance and development of Laves phase particles, which are large and hard, and have difficulty being coherent with the matrix during the deformation process. The coarsened particles facilitated the crack initiation and propagation, corresponding to the TEM results in Figure 9. The comprehensive effects of the precipitation of the Laves phase (negative effect, Figure 9), increase in HAGB (positive effect, Figure 7), and the softening of the metal matrix (positive effect) led to the impact toughness of the steel basically staying constant from 500 to 10,000 h.

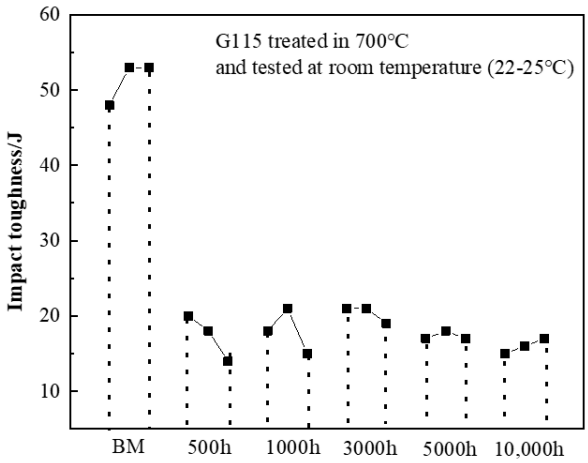


Figure 10. Impact energy evolution of the G115 steel after long-term aging at 700 °C.

Table 1. Statistical analysis of the impact toughness results of the G115 steel after long-term aging at 700 °C.

Impact Toughness Results	BM	500 h	1000 h	3000 h	5000 h	10,000 h
Minimum value (J)	48.5	14.8	14.9	19.2	16.5	15.3
Maximum value (J)	53.6	20.1	21.6	21.8	17.1	16.8
Mean value (J)	51.3	17.4	18.2	19.6	16.7	15.7

Figure 11 presents the impact fracture for G115 steel after a long-term aging process, including the radiation area and the fiber region. The higher the fraction of fiber region, the better the toughness. The section rate of the fiber region in the fracture is about 70% for BM, which is about 45–55% for the G115 steel after the aging process at 700 °C. There are many dimples in the fiber region for all specimens, while the pore size of the fiber zone gradually decreased with aging time, which indicates the decrease in toughness for G115 steel during the long-term aging process. River patterns can be observed in the radiation area for all specimens, which indicates a typical cleavage fracture characteristic. The cleavage fracture characteristic became obvious with aging time, which indicates the decreasing toughness of G115 steel [18,21]. The counteracting effects of the precipitation of the Laves phase, the decrease in large-angle boundaries (negative effect), and the softening of the metal matrix (positive effect) led to the toughness of the steel decreasing rather slowly from 1000 to

5000 h. Combined with EBSD and TEM results, the Laves phase particles with large size acted as the main factor reducing the toughness, which destroyed the stabilization of the microstructure and weakened its ability to resist the local plastic deformation.

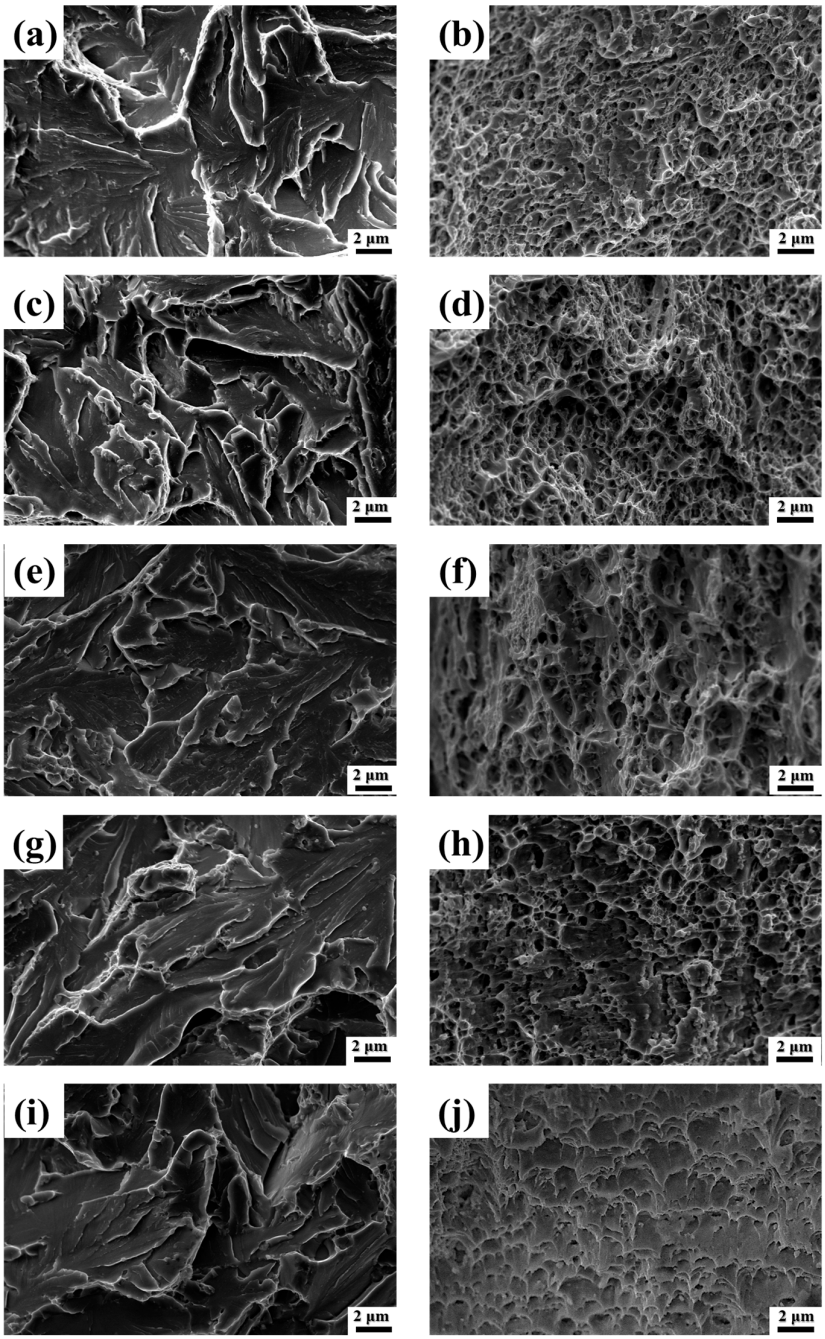


Figure 11. SEM micrographs of the impact fracture for G115 steel with different aging times at 700 °C: ((**a**) radiation area, (**b**) fiber region) BM, ((**c**) radiation area, (**d**) fiber region) 500 h, ((**e**) radiation area, (**f**) fiber region) 3000 h, ((**g**) radiation area, (**h**) fiber region) 5000 h, and ((**i**) radiation area, (**j**) fiber region)) 10,000 h.

4. Conclusions

How the microstructure and toughness of G115 steel evolved during the aging process at 700 °C was systematically investigated in this work. It can be concluded that the microstructure of the G115 steel evolved significantly with increasing aging time at 700 °C, demonstrating that the microstructure consisted of a coarse-grained matrix with minor

precipitates. The precipitates began to grow and coarsen with time, resulting in a finer-grained matrix with more extensive precipitate growth. The impact toughness of the steel presents a sharp decline from 51.3 J to 17.4 J at the initial aging time relating to the formation of particles, and an unobvious numerical fluctuation at about 17 J from 500 h to 100,000 h aging times. The decrease in impact toughness was attributed to the coarsening of Laves phase particles with large sizes in the steel matrix, which decreased the local plastic deformation resistance.

Author Contributions: Conceptualization: J.Y. and S.M.; methodology, K.L.; software, K.L.; validation, J.Y. and S.M.; formal analysis, S.M.; investigation, S.M.; writing—original draft preparation, J.Y. and S.M.; writing—review and editing, K.Y.; visualization, X.Y.; supervision, S.Z.; project administration, S.M.; funding acquisition, J.Y. All authors have read and agreed to the published version of the manuscript.

Funding: This work is financially supported by the National Key Research and Development Program of China (2021YFC3001805).

Data Availability Statement: The data presented in this study are available on request from the corresponding author. The data are not publicly available due to technical or time limitations.

Conflicts of Interest: Authors were employed by the company China Special Equipment Inspection and Research Institute. The authors declare that the research was conducted in the absence of any commercial or financial relationships that could be construed as a potential conflict of interest.

References

1. Abe, F. Precipitate design for creep strengthening of 9% Cr tempered martensitic steel for ultra-supercritical power plants. *Sci. Technol. Adv. Mater.* **2008**, *9*, 013002. [CrossRef] [PubMed]
2. Chen, Y.D.; Chen, X.D.; Jiang, H.F.; Chen, C.G.; Zhang, X.A. Design technology of large-scale spiral wound heat exchanger in refinery industry. *Proc. Eng.* **2015**, *130*, 286–297. [CrossRef]
3. Yang, Z.H.; Liu, B.; Zhao, H.C.; Li, J.F.; Guo, X.H.; Zhang, D.Q.; Liu, Z.H. Pyrolysis mechanism of composite binder composed of coal tar pitch and phenolic resin for carbon materials. *J. Anal. Appl. Pyrolysis* **2023**, *169*, 105840. [CrossRef]
4. Yang, X.J.; Liu, M.H.; Liu, Z.Y.; Du, C.W.; Li, X.G. Failure analysis of a 304 stainless steel heat exchanger in liquid sulfur recovery units. *Eng. Fail. Anal.* **2020**, *116*, 104729. [CrossRef]
5. Hamaguchi, T.; Kurihara, S.; Hirata, H.; Okada, H. Creep rupture properties and microstructures of 9Cr-3Co-3W-Nd-B steel welded joints. *Mater. Sci. Eng. A* **2022**, *831*, 142231. [CrossRef]
6. Panait, C.G.; Zielinska-Lipiec, A.; Koziel, T.; Czyrska-Filemonowicz, A.; Gourgues-Lorenzon, A.-F.; Bendick, W. Evolution of dislocation density, size of subgrains and MX-type precipitates in a P91 steel during creep and during thermal ageing at 600 C for more than 100,000 h. *Mater. Sci. Eng. A* **2010**, *527*, 4062. [CrossRef]
7. Sellars, C.M.; Whiteman, J.A. Recrystallization and grain growth in hot rolling. *Met. Sci.* **1978**, *13*, 187–194. [CrossRef]
8. Semba, H.; Abe, F. Alloy design and creep strength of advanced 9% Cr USC boiler steels containing high concentration of boron. *Energy Mater.* **2006**, *1*, 238–244. [CrossRef]
9. Zhang, T.; Liu, W.; Sun, Y.; Dong, B.; Yang, W.; Chen, L. Investigating the corrosion resistance of Cu-doped Ni-Mo low alloy steel through electrochemical tests. *Corros. Commun.* **2023**, *10*, 10–26. [CrossRef]
10. Wen, J.F.; Tu, S.T. A multiaxial creep-damage model for creep crack growth considering cavity growth and microcrack interaction. *Eng. Fract. Mech.* **2014**, *123*, 197–210. [CrossRef]
11. Muhammed, M.; Mustapha, M.; Ginta, T.L.; Ali, A.M.; Mustapha, F.; Hampo, C.C. Statistical review of microstructure-property correlation of stainless steel: Implication for pre-and post-weld treatment. *Processes* **2020**, *8*, 811. [CrossRef]
12. Niu, J.W.; Wang, Z.F.; Liu, H.; Ma, Y.; Pang, H.X.; Wang, X.T. Response surface optimization of pitch phase change densification using composite phenolic resin co-carbonization to prepare high performance carbon refractories. *J. Anal. Appl. Pyrolysis* **2023**, *175*, 106144. [CrossRef]
13. Yoon, K.B.; Saxena, A.; Liaw, P.K. Characterization of creep-fatigue crack growth behavior under trapezoidal waveshape using C *t* -parameter. *Int. J. Fract.* **1993**, *16*, 95–114. [CrossRef]
14. Zhang, T.; Liu, W.; Dong, B.; Yang, W.; Chen, L.; Sun, Y.; Li, H.; Zhang, B. Clarifying the effect of Cu element on the corrosion properties of Ni-Mo low alloy steel in marine environment. *Corros. Sci.* **2023**, *216*, 111107. [CrossRef]
15. Xu, L.; Zhao, L.; Gao, Z.; Han, Y. A novel creep-fatigue interaction damage model with the stress effect to simulate the creep-fatigue crack growth behavior. *Int. J. Mech. Sci.* **2017**, *130*, 143–153. [CrossRef]
16. Yan, P.; Liu, Z.; Bao, H.; Weng, Y.; Liu, W. Effect of normalizing temperature on the strength of 9Cr-3W-3Co martensitic heat resistant steel. *Mater. Sci. Eng. A* **2014**, *597*, 148–156. [CrossRef]
17. Zhang, T.; Liu, W.; Dong, B.; Mao, R.; Sun, Y.; Chen, L. Corrosion of Cu-doped Ni–Mo low-alloy steel in a severe marine environment. *J. Phys. Chem. Solids* **2022**, *163*, 110584. [CrossRef]

18. Zhao, L.; Xu, L.; Nikbin, K. Predicting failure modes in creep and creep-fatigue crack growth using a random grain/grain boundary idealised microstructure meshing system. *Mater. Sci. Eng. A* **2017**, *704*, 274–286. [CrossRef]
19. Zhao, L.; Jing, H.; Han, Y.; Xiu, J.; Xu, L. Prediction of creep crack growth behavior in ASME P92 steel welded joint. *Comput. Mater. Sci.* **2012**, *61*, 185–193. [CrossRef]
20. Calderón, L.A.Á.; Rehmer, B.; Schriever, S.; Ulbricht, A.; Jácome, L.A.; Sommer, K.; Mohr, G.; Skrotzki, B.; Evans, A. Creep and creep damage behavior of stainless steel 316L manufactured by laser powder bed fusion. *Mater. Sci. Eng. A* **2022**, *830*, 142223. [CrossRef]
21. Abe, F. Effect of fine precipitation and subsequent coarsening of Fe2W laves phase on the creep deformation behavior of tempered martensitic 9Cr-W steels. *Metall. Mater. Trans. A* **2005**, *36*, 321–332. [CrossRef]
22. Zhang, T.; Liu, W.; Khan, H.I.; Dong, B.; Yang, W.; Sun, Y.; Zhang, B.; Chen, L.; Li, H. Effects of Cu on the corrosion resistance of heat-treated weathering steel in a marine environment. *Mater. Today Phys.* **2023**, *36*, 101160. [CrossRef]
23. Yan, P.; Liu, Z.; Bao, H.; Weng, Y.; Liu, W. Effect of microstructural evolution on high temperature strength of 9Cr-3W-3Co martensitic heat resistant steel under different aging conditions. *Mater. Sci. Eng. A* **2013**, *588*, 22–28. [CrossRef]
24. Gao, Q.; Dong, X.; Li, C.; Lin, Z.; Yang, X.; Dai, M. Microstructure and oxidation properties of 9Cr-1.7W-0.4Mo-Co ferritic steel after isothermal aging. *J. Alloys Compd.* **2015**, *651*, 537–543. [CrossRef]
25. *GB/T 229-2007*; Metallic Materials-Charpy Pendulum Impact Test Method. National Standard of the People's Republic of China: Beijing, China, 2007.
26. Xiao, B.; Xu, L.; Zhao, L.; Jing, H.; Han, Y.; Tang, Z. Microstructure evolution and fracture mechanism of a novel 9Cr tempered martensite ferritic steel during short term creep. *Mater. Sci. Eng. A* **2017**, *707*, 466–477. [CrossRef]
27. Jiang, H.T.; Wang, Y.X.; Wang, C.J.; Li, M.F.; Xu, Z.H. Catalyst optimization and reduction condition of continuous growth of carbon nanotubes on carbon fiber surface. *Ceram. Int.* **2023**, *49*, 25469–25476. [CrossRef]
28. Wen, J.F.; Srivastava, A.; Benzerga, A.; Tu, S.T.; Needleman, A. Creep crack growth by grain boundary cavitation under monotonic and cyclic loading. *J. Mech. Phys. Solids* **2017**, *108*, 68–84. [CrossRef]
29. Msuyama, F. History of power plants and progress in heat resistant steels. *ISIJ Int.* **2007**, *41*, 612–625. [CrossRef]

Disclaimer/Publisher's Note: The statements, opinions and data contained in all publications are solely those of the individual author(s) and contributor(s) and not of MDPI and/or the editor(s). MDPI and/or the editor(s) disclaim responsibility for any injury to people or property resulting from any ideas, methods, instructions or products referred to in the content.